Observation of enhanced X-ray emission from the CTTS AA Tau during a transit of an accretion funnel flow[⋆]

N. Grosso[1], J. Bouvier[2], T. Montmerle[2], M. Fernández[3], K. Grankin[4], and M.R. Zapatero Osorio[5]

[1] Observatoire astronomique de Strasbourg, Université Louis-Pasteur, CNRS, INSU, 11 rue de l'Université, 67000 Strasbourg, France
[2] Laboratoire d'astrophysique de Grenoble, Université Joseph-Fourier, CNRS, INSU, 414 rue de la Piscine, 38041 Grenoble, France
[3] Instituto de Astrofísica de Andalucía, CSIC, Camino Bajo de Huétor 50, 18008 Granada, Spain
[4] Ulugh Beg Astronomical Institute of the Uzbek Academy of Sciences, Astronomicheskaya 33, 700052 Tashkent, Uzbekistan
[5] Instituto de Astrofísica de Canarias (IAC), vía Láctea s/n, 38205 La Laguna, Tenerife, Spain

ABSTRACT

Context. Classical T Tauri stars are young solar-type stars accreting material from their circumstellar disks. Thanks to a favorable inclination of the system, the classical T Tauri star AA Tau exhibits periodic optical eclipses as the warped inner disk edge occults the stellar photosphere.
Aims. We intend to observe the X-ray and UV emission of AA Tau during the optical eclipses with the aim to localize these emitting regions on the star.
Methods. AA Tau was observed for about 5 h per *XMM-Newton* orbit (2 days) over 8 successive orbits, which covers two optical eclipse periods (8.22 days). The *XMM-Newton* optical/UV monitor simultaneously provided UV photometry (UVW2 filter at 206 nm) with a ~15 min sampling rate. Some *V*-band photometry was also obtained from the ground during this period in order to determine the dates of the eclipses.
Results. Two X-ray and UV measurements were secured close to the center of the eclipse ($\Delta V \sim 1.5$ mag). The UV flux is the highest just before the eclipse starts and the lowest towards the end of it. UV flux variations amount to a few 0.1 mag on a few hours timescale, and up to 1 mag on a week timescale, none of which are correlated with the X-ray flux. We model it with a weekly modulation (inner disk eclipse), plus a daily modulation, which suggests a non-steady accretion, but needs a longer observation to be confirmed. No such eclipses are detected in X-rays. Within each 5 h-long observations, AA Tau has a nearly constant X-ray count rate. On a timescale of days to weeks, the X-ray flux varies by a factor of 2–8, except for one measurement where the X-ray count rate was nearly 50 times stronger than the minimum observed level even though photoelectric absorption was the highest at this phase, and the plasma temperature reached 60 MK, i.e. a factor of 2–3 higher than in the other observations. This X-ray event, observed close to the center of the optical eclipse, is interpreted as an X-ray flare.
Conclusions. We identify the variable column density with the low-density accretion funnel flows blanketing the magnetosphere. The lack of X-ray eclipses indicates that X-ray emitting regions are located at high latitudes. Furthermore, the occurrence of a strong X-ray flare near the center of the optical eclipse suggests that the magnetically active areas are closely associated with the base of the high-density accretion funnel flow. We speculate that the impact of this free falling accretion flow onto the strong magnetic field of the stellar corona may boost the X-ray emission.

Key words. Stars: individual: AA Tau – Stars: pre-main sequence – Stars: flare – X-rays: stars – Accretion, accretion disks

1. Introduction

T Tauri stars (TTSs), i.e. young (1–10 Myrs) solar-type stars, are conspicuous X-ray emitters. Their high X-ray luminosities ($L_X \simeq 10^{28-31}$ erg s^{-1}) compared to the Sun ($L_X \simeq 10^{27}$ erg s^{-1} at solar maximum), and intense flaring activity (up to $L_X \simeq 10^{32-33}$ erg s^{-1}) make them appear as extremely active young Suns in the X-ray domain. The analogy with the solar activity has been quite successful in ascribing the X-ray emission of TTSs to an optically thin, magnetically confined coronal plasma in collisional equilibrium at temperatures of 10–100 MK, emitting a thermal bremsstrahlung continuum and emission lines (see, e.g., review by Feigelson & Montmerle 1999). As observed in the X-ray coronae of active stars (e.g., Ness et al. 2004), the enhanced X-ray luminosity of TTSs can easily be explained by coronal structures with high plasma density, because

the X-ray luminosity is proportional to the plasma emission measure, which scales linearly with the plasma volume but with the square of the plasma electronic density. That most of TTSs X-ray emission arises in an active magnetic corona is supported by direct Zeeman measurements on photospheric spectral lines which indicate surface magnetic fields of a few kilogauss (e.g., Guenther et al. 1999; Johns-Krull et al. 1999, 2004; Johns-Krull 2007; Yang et al. 2005). However, the dynamo mechanism producing the magnetic field in these fully convective stars is still discussed (e.g., Preibisch et al. 2005; Briggs et al. 2007).

The solar paradigm, where the X-ray emitting plasma is confined in magnetic loop with both feet anchored on the stellar photosphere, has been questionned in the context of a Classical TTS (CTTS), which accretes material from its circumstellar disk. Inside a few stellar radii above the CTTS surface, the stellar magnetic field pressure is larger than the ram pressure of the accreting gas. As a result, the stellar magnetosphere truncates the inner accretion disk and controls the accretion flows. The gas is

---

[⋆] Figures 2, 3 and 9, and Appendix A are only available in electronic form via http://www.edpsciences.org .

mainly accreted from the disk edge to the stellar surface along the dominant large scale stellar magnetic lines, creating accretion funnel flows. The free-falling gas hits the stellar surface at the feet of the accretion funnel flows, where the kinetic energy is dissipated in a shock producing hot excess emission (see review on magnetospheric accretion by Bouvier et al. 2007b).

The X-ray grating spectrometers aboard *Chandra* and *XMM-Newton* are able to obtain spectra of the X-ray brightest CTTSs, where the emission line triplets of He-like elements are resolved, which provides a powerful tool to assess the electronic density of the X-ray emitting plasma (e.g., Porquet et al. 2001). In several CTTSs, plasma with high electronic density ($n_e \sim 10^{13}$ cm^{-2}) and low temperature ($\sim$3 MK), untypical of stellar coronae, were identified, and therefore attributed to accretion shocks (Kastner et al. 2002; Stelzer & Schmitt 2004; Schmitt et al. 2005; Robrade & Schmitt 2006; Argiroffi et al. 2007; Günther et al. 2007; Telleschi et al. 2007); whereas some CTTSs display no such evidence (Audard et al. 2005; Smith et al. 2005; Güdel et al. 2007b).

During the *Chandra Orion Ultradeep Project* (COUP, see Getman et al. 2005b), where the TTSs of the Orion nebula cluster were monitored nearly continuously over $\sim$13 days with the *Advanced CCD Imaging Spectrometer*, numerous X-ray flares were observed. In a few cases, a size of several stellar radii was derived for the magnetic loop confining the X-ray emitting plasma, large enough to connect the stellar surface with the edge of the accretion disk (Favata et al. 2005).

We propose to directly constrain the source and location of the X-ray emission in CTTSs by using eclipses. Eclipse mapping have been successfully used in binary active stars to reconstruct the coronae (e.g., Güdel et al. 2001, 2003), or to localize the flaring plasma (e.g., Schmitt & Favata 1999; Schmitt et al. 2003). Our target star is AA Tau, located in the Taurus molecular cloud complex at a distance of $\sim$140 pc (e.g., Kenyon et al. 1994). AA Tau is a quite typical member of the CTTS class, with a K7 spectral type, a bolometric luminosity of $\sim$0.8 L$_\odot$, a stellar mass of $\sim$0.8 M$_\odot$, and a stellar radius of $\sim$1.85 R$_\odot$; exhibiting moderate accretion disk diagnostics (near-IR excess, optical veiling, Balmer line emission), but with the remarkable property to be viewed nearly edge-on. Bouvier et al. (1999, 2003, 2007a) reported evidence for a modulation of the photospheric flux and spectroscopic diagnostics with a period of 8.22 days, corresponding to the rotational period of the star. This stellar flux modulation was interpreted as the periodic eclipse of the stellar photosphere by the optically thick, magnetically-warp inner disk edge located at 8.8 stellar radii. Photopolarimetric variations confirm the presence of an optically thick wall located at the disk edge, and eclipsing periodically the stellar photosphere (Ménard et al. 2003).

We obtained 8 observations of AA Tau with *XMM-Newton* (Jansen et al. 2001), which allows simultaneous observations with an EPIC pn (Strüder et al. 2001) and two EPIC MOS (Turner et al. 2001) X-ray spectroimaging cameras, and the Optical/UV monitor (OM; Mason et al. 2001). We supplemented these X-rays and UV observations with an optical ground-based monitoring of AA Tau to secure the dates of the optical eclipses. These *XMM-Newton* observations were previously reported in Schmitt & Robrade (2007, hereafter SR), who used the minimum of the UV light curve as proxy of the optical eclipse. SR found variable X-ray absorption "such that the times of maximal X-ray absorption and UV extinction coincide". SR introduced an additional absorption in a disk wind, or a peculiar dust grain distribution to reconcile the high value of the X-ray absorption outside the eclipse and the low optical extinction.

Table 1. Journal of the *XMM-Newton* observations of AA Tau (PI: J. Bouvier).

Obs.	Rev.	ObsId	Feb. 2003[a] (d)	Exposure[a] (h)
1	583	015680201	14.10–14.29	4.7
2	584	015680301	16.13–16.33	4.7
3	585	015680501	18.07–18.26	4.7
4	586	015680401	20.02–20.22	4.7
5	587	015680601	22.13–22.35	5.4
6	588	015680701	24.03–24.25	5.3
7	589	015680801	26.52–26.71	4.6
8	590	015680901	28.30–28.50	4.7

[a] The observation beginning, end, and duration is given for MOS1.

In Sect. 2, we present the X-ray and UV properties of AA Tau based on a reanalysing of the full data set provided by these *XMM-Newton* observations. In particular, we report X-ray (pn+MOS1+MOS2) and UV light curves with a time resolution of $\sim$15 min. We show that a bright and hot flare was observed during the second observation. In Sect. 3, thanks to our ground-based observations and optical OM data, we determine the dates of the optical eclipses, which allow us to compare the UV and X-ray variabilities versus the rotational phase. We show that the UV minimum is outside the eclipse, and that the (confirmed) variation of the column density are not correlated with the rotational phase. In Sect. 4, we propose another origin for this variable column density, and we discuss the origin of the X-ray flare that was observed during an optical eclipse.

2. X-ray and UV properties of AA Tau

2.1. XMM-Newton observations and event selections

Our observational strategy with *XMM-Newton* was to cover two consecutive modulation periods ($\sim$17 days) in order to demonstrate the reproducibility of the phenomenon from one rotational cycle to the next. The temporal sampling of the X-ray light curve needs not to be very dense because AA Tau spends nearly the same amount of time being eclipsed as being entirely visible. Therefore, we requested one 4 h-exposure with EPIC pn per *XMM-Newton* orbit (2 days) over 8 successive orbits. We used the full frame science mode of the EPIC cameras with the medium optical blocking filter. The pointing nominal coordinates were 04^{h}34^{m}55^{s}5, 24°28′54″0 (J2000 equinox). The journal of the *XMM-Newton* observations of AA Tau is given in Table 1.

The data reduction was made using the *XMM-Newton* Science Analysing System (SAS, version 7.0.0) For each observations, the event lists for each camera of EPIC were produced using the SAS tasks `epchain` and `emchain`, respectively. We used the background lightcurves computed by these task in the 7.0–15.0 keV energy range to determine the time intervals affected by background proton flares. More than half of the observing time is affected by bad space weather. For each instrument, we made from the low background time intervals a sky image with 3″-pixels in the 0.5–7.3 keV energy range[1]. The X-ray counterpart of AA Tau was detected in all the observations.

[1] We selected single, double, triple, and quadruple pixel events (i.e. `PATTERN` in the 0 to 12 range), and also applied the predefined filter `#XMMEA_EM` for MOS.
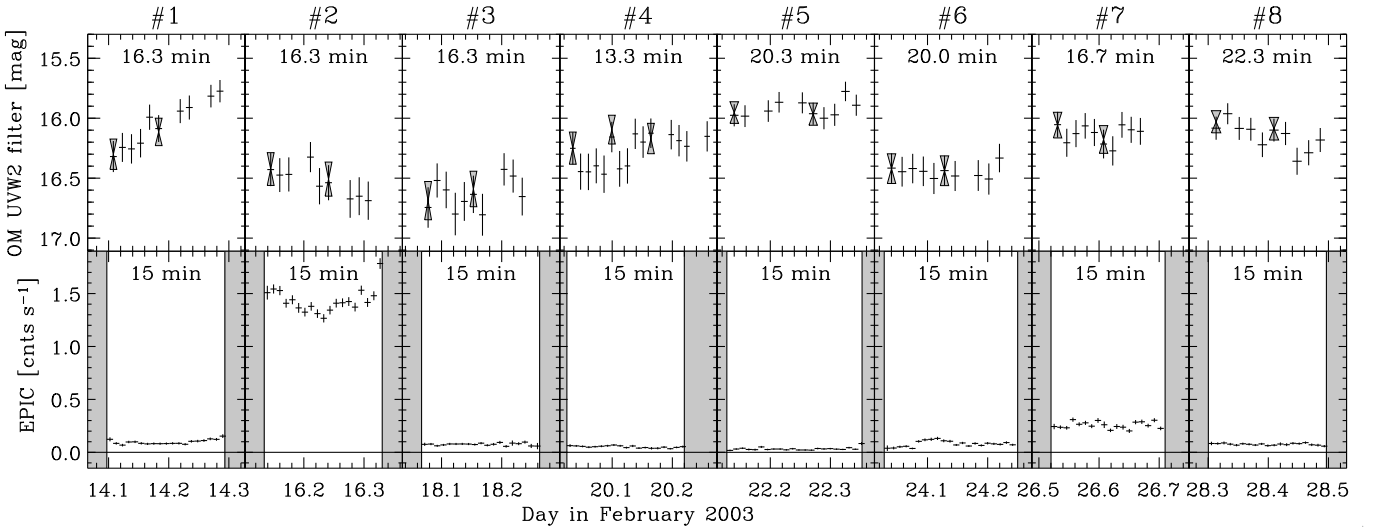
Fig. 1. *XMM-Newton* observations of AA Tau. Top and bottom panels show the background subtracted UV (180–250 nm) and X-ray (0.5–7.3 keV) light curves obtained with the Optical/UV Monitor (OM) and EPIC (pn+MOS1+MOS2), respectively. In each panel, the label indicates the time interval used to bin the light curve. Grey hourglasses and crosses data points indicate UV photometry obtained with the large and small OM central imaging window. The X-ray count rates are corrected from (circular) aperture. The gray stripes indicate the beginning and the end of the EPIC observation.

For the X-ray light curves of AA Tau, we selected the source+background events within a circular region centered on AA Tau . The extraction position and radius were optimized to maximize the signal-to-noise ratio in the sky image. The background in MOS and pn was extracted using an annular region centered on AA Tau and a box region at the same distance to the CCD readout node, respectively, where areas illuminated by other weak X-ray sources were excluded. For the X-ray spectra, we used the same extraction regions and only time intervals with low background; we selected events with energy above 0.3 keV and the usual stronger selection criteria[2]. We computed the corresponding redistribution matrix files and ancillary response files.

2.2. X-ray light curves

For each instrument and observations, we first built the source+background and the background light curves with 1 s time bins starting at the first good time interval (GTI) of MOS1. We rebinned the light curve to 900 s to increase the signal. Then, we subtracted from the source+background light curve the background light curve scaled to the same source extraction area.

From the GTI extension, we scaled up with an IDL routine count rates and errors affected by any lost of observing time, mainly due to the triggering of counting mode during high flaring background periods, when the count rate exceeded the detector telemetry limit. We also corrected count rates and errors for circular aperture photometry using the fraction of PSF counts inside the (circular) extraction region calculated by the SAS assuming a fixed photon energy of 1.5 keV. Finally, the light curves of the three detectors were summed to produce the EPIC light curves. We estimated the missing pn data at the beginning of the observations by multiplying the MOS1+MOS2 count rates by

1.17, the median scaling factor between MOS1+MOS and pn in the second observation where AA Tau was the brightest.

The bottom panel of Fig. 1 shows the EPIC light curves of AA Tau in the 0.5–7.3 keV energy range. Within each 5 h-long observations, AA Tau exhibited a nearly constant X-ray flux. The minimum X-ray flux, that we will call hereafter the quiescent level, was observed during the observation #5, where the averaged EPIC count rate was 0.030 ± 0.002 counts s^{-1}. On a timescale of days to weeks, the X-ray flux varies by a factor of 2–8, except between the end of the first observation and the beginning of the second observation, where the EPIC count rate jumped in less than 2 days from 0.093 ± 0.003 to 1.42 ± 0.01 counts s^{-1}, i.e. a level 47 ± 3 times stronger than the quiescent level. Then, the EPIC count rate decayed in less than 2 days to 0.075 ± 0.003 counts s^{-1}, i.e. a level only 2.5 ± 0.2 times stronger than the quiescent level.

Such large amplitudes in the X-ray fluxes of young stellar objects are usually observed during X-ray flares, which have typical light curves with fast rise and peak phase, and slower (exponential) decay phase, associated with fast heating and slow cooling of the magnetically confined plasma (e.g., Imanishi et al. 2003; Favata et al. 2005). X-ray flares with unusually long rise phases have also been reported (e.g., Grosso et al. 2004; Wang et al. 2007; Broos et al. 2007).

For a comparison purpose, we note that, assuming a typical convertion ratio between *XMM-Newton*/EPIC and *Chandra*/ACIS-I count rates (e.g., Ozawa et al. 2005), the average EPIC count rate of AA Tau, ~0.08 counts s^{-1} at the distance of the Taurus molecular cloud ($d \sim 140$ pc), would convert to ~0.001 *Chandra*/ACIS-I counts s^{-1} at the distance of the Orion nebula ($d \sim 450$ pc). AA Tau, put in the Orion nebula cluster, would have then been brighter than 67% of the X-ray sources in the COUP. To check whether the behaviour of the light curve of AA Tau is consistent with the one of an X-ray flare, we can compare it to the light curve data set obtained in the COUP.

We use the COUP results of the Bayesian block (BB) variability analysis (developed by Scargle 1998; adapted for the COUP data set and coded in IDL by one of us, N.G.), which segmented the X-ray light curves into a contiguous sequences

---

[2] For pn, we selected only single and double pixel events (i.e. PATTERN in the 0 to 4 range) with FLAG value equal to zero; for MOS, we selected PATTERN in the 0 to 12 range, and applied the predefined filter #XMMEA_SM.

Table 2. Best parameters of simultaneous fitting of EPIC pn, MOS1, MOS2 spectra with XSPEC.

Obs.	Rate[a] (cnts s^{-1})	N_H (10^{22} cm^{-2})	Plasma temperature		Emission measure		Goodness-of-fit		Flux[b]	Intrinsic luminosity			η[c]
			T_1	T_2	EM_1	EM_2	χ^2_ν (ν)	Q		0.5–2, 2–8, 0.5–8 keV			
			(MK)		(10^{53} cm^{-3})			(%)		(10^{30} erg s^{-1})			
1	0.057	0.95	....	25.9	....	1.0	0.93 (50)	61	1.9	0.6	0.4	0.9	-3.5
	±0.002	0.87–1.02	....	23.9–28.4	....	0.9–1.0							
2	0.800	1.54	....	43.9	....	14.0	1.09 (599)	5	37.8	8.2	9.2	17.4	-2.2
	±0.008	1.51–1.57	....	42.7–45.2	....	13.6–14.3							
2	0.800	1.80	14.6	59.4	9.8	9.3	1.03 (597)	28	37.9	11.8	9.5	21.3	-2.2
	±0.008	1.75–1.85	13.4–15.7	54.6–66.0	8.8–10.7	7.8–10.8							
3	0.046	1.36	....	20.8	....	1.1	1.21 (30)	20	1.6	0.7	0.3	1.0	-3.5
	±0.002	1.23–1.51	....	18.4–23.4	....	1.0–1.3							
4	0.031	1.33	....	21.5	....	0.8	0.79 (25)	76	1.1	0.5	0.2	0.7	-3.6
	±0.002	1.17–1.52	....	18.7–24.8	....	0.6–0.9							
5	0.019	1.04	....	22.6	....	0.4	1.32 (15)	18	0.7	0.2	0.1	0.4	-3.9
	±0.002	0.85–1.27	....	18.3–28.8	....	0.3–0.5							
6	0.050	1.54	....	40.5	....	0.9	1.20 (39)	18	2.3	0.5	0.5	1.1	-3.5
	±0.002	1.40–1.72	....	34.6–47.4	....	0.8–1.0							
7	0.147	1.02	....	44.8	....	2.1	1.05 (110)	33	6.5	1.2	1.4	2.6	-3.1
	±0.005	0.97–1.08	....	41.3–48.6	....	2.0–2.2							
8	0.043	1.53	....	23.3	....	1.2	1.19 (29)	23	1.8	0.7	0.4	1.1	-3.4
	±0.002	1.39–1.69	....	20.7–26.5	....	1.0–1.4							

Notes: We fit the X-ray spectra with the continuum and emission lines produced by an optically thin plasma in thermal collisional ionization equilibrium model (vapec). We use for the plasma element abundances typical values observed in the coronae of young stars with fine X-ray spectroscopy (Güdel et al. 2007a, see Table A.1). The wabs photoelectric absorption model use photoionization cross sections of Morrison & McCammon (1983), and solar abundances of Anders & Grevesse (1989). Errors are given at the 68% confidence level (i.e. $\Delta\chi^2 = 1.0$ for each parameter of interest), that corresponds to 1σ for Gaussian statistics. For observation #2, a better fit is obtained using a plasma with two temperature components.

[a] pn count rate (0.2–12 keV).
[b] Observed X-ray flux (0.5–8.0 keV) in unit of 10^{-13} erg cm^{-2} s^{-1}.
[c] Logarithm of the X-ray intrinsic luminosity (0.5–8 keV) to the bolometric luminosity (0.8 $L_\odot$) ratio.

of constant count rates (see Getman et al. 2005b). We define a source to be variable, if there is more than one BB; with BB_{min} and BB_{max}, the minimum and the maximum count rate levels, respectively (see, e.g., Stassun et al. 2007, for an application of COUP time-averaged X-ray variability). The latter and the former are viewed as the quiescent level and the peak level of the brightest flare, respectively. Applying this criteria, there are 977 variable sources (out of 1616 COUP sources). We find only 20 variable sources with peak amplitude (BB_{max}/BB_{min}) and duration larger than 45 and 4.7 h., respectively, as observed for AA Tau. For comparison, our subsample sources have $BB_{max} = 10^{-4}$–2 counts s^{-1}, i.e., they are at peak between 200 times fainter and 100 times brighter than AA Tau (at the distance of the Orion nebula) at peak.

Then, we make a visual examination of the selected BB light curves to eliminate sources with peak flare BB having a spurious long duration (including for example a passage through the van Allen belts), and/or sources with a decay phase too slow to reproduce the level observed at the beginning of the third observation of AA Tau. For an exponential decay phase with a decay timescale τ_d, this latter criteria is equivalent to $\tau_d < 0.6$ day. Finally, we exhibit the brightest flares from COUP 313, 874, and 970, which fullfill our criteria (see online Fig. 2). These sources are bona fine members of the Orion nebula cluster (Getman et al. 2005a).

We conclude that a bright X-ray flare with a rapid cooling phase can well reproduce the large amplitude, and also the flatness of the light curve of AA Tau at its maximum. The following X-ray spectra analysis confirms this interpretation.

2.3. X-ray spectra and plasma parameters

For each observations the pn, MOS1, and MOS2 spectra were binned to 25 counts per spectral bin. X-rays are detected up to 10 keV (see online Fig. 3). The spectra are featureless, except in the second observation where a prominent line around 6.7 keV is visible both in the pn and MOS spectra, corresponding to the Fe XXV triplet emission line (Fig. 4).

The pn, MOS1, and MOS2 spectra were fitted simultaneously with XSPEC (version 12.3.0; Dorman & Arnaud 2001) to derive the plasma parameters. The model is an X-ray emission spectrum from collisionally-ionized diffuse gas, output from the Astrophysical Plasma Emission Code (vapec[3]), that includes continuum and emission lines. The plasma element abundances were fixed to typical values measured in the coronae of young stars with grating X-ray spectroscopy (see online appendix Table A.1), to allow a direct comparison with the *XMM-Newton Extended Survey of the Taurus molecular cloud* (XEST; Güdel et al. 2007a). This emission model is combined with the wabs photoelectric absorption model, which is based on the photoionization cross sections of Morrison & McCammon (1983), and the solar abundances of Anders & Grevesse (1989). The online Fig. 3 shows our best fits. For the second observation, we find a better fit by adding a second temperature component, which reduced the χ^2 from 655.4 (for 599 degrees of freedom; d.o.f.) to 617.2 (for 597 d.o.f.). Given the new and old values of χ^2 and number of degrees of freedom, a F-test indicates a probability of $\sim10^{-8}$ for the null hypothesis; therefore, we conclude

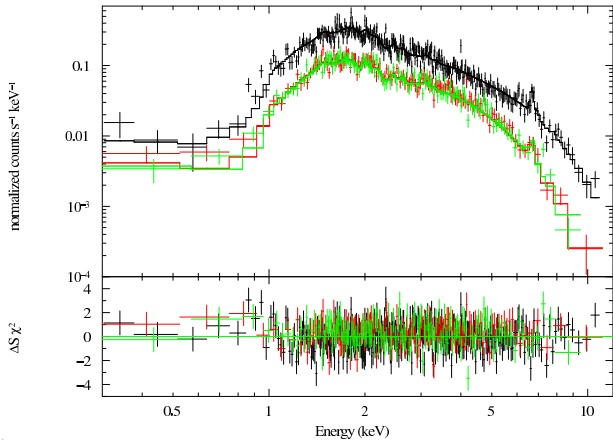[3] More information can be found at: http://hea-www.harvard.edu/APEC/sources_apec.html .

Fig. 4. EPIC pn (black), MOS1 (red), MOS2 (green) spectra of AA Tau for observation #2. The lines show our best fit using two temperature plasma combined with photoelectric absorption (Table 2). The residuals are plotted in sigma units with error bars of size one.

that it is reasonnable to add this extra temperature component to improve the fit. Our best fit with a two-temperature plasma is shown in Fig. 4.

Table 2 gives the corresponding plasma parameters. On timescale of 2-days, the photoelectric absorption of the X-ray spectra is not constant, but the observed relative variations are lower than a factor of two. The minimum and maximum values of the corresponding column density are $\sim 1.0 \times 10^{22}\,cm^{-2}$ and $1.8 \times 10^{22}\,cm^{-2}$, respectively; the latter was observed during the second observation[4]. SR didn't specify the model of X-ray absorption that they used, but their one-temperature plasma model gave qualitatively similar results. We stress that the value of the column density can even be increased by 50% when revised solar abundances (i.e., metal poor) are adopted for the abundances of the absorbing material (see online Appendix A).

The plasma temperature is $\sim 23\,MK$ during the low activity levels. The observations showing an increase of X-ray count rates (namely #2, #6, and #7) also correspond to phases with the highest plasma temperatures (60 MK, 40 MK, and 45 MK, respectively), and therefore to flaring activity.

During the second observation the X-ray surface flux, i.e., the intrinsic X-ray luminosity divided by the stellar surface, peaked to $10^8\,erg\,s^{-1}\,cm^{-2}$. The temperatures of the hot (60 MK) and cool (15 MK) plasma components, associated with this elevated level of X-ray surface flux, are consistent with the ones observed in the most active TTSs of COUP (see Fig. 11 of Preibisch et al. 2005). The cool plasma component is usually observed in the coronae of active stars, and may define a fundamental coronal structure, which is probably related to a class of compact loops with high plasma density (see Preibisch et al. 2005, and references therein).

We make an estimate of the hot loop length using the method of Reale et al. (1997) (see also Favata et al. 2005, for an application on COUP data). Assuming a peak temperature of 60 MK and a flare decay time lower than 0.6 day (see Sect. 2.2), we find for the semi-circular loop a half-length lower than $7.1\,R_\star$ for a freely decaying loop, with no heating; or lower than $1.6\,R_\star$ for

a strongly sustained heating[5] in the cooling phase. Therefore, the height of the semi-circular loop is lower than $1-4.5\,R_\star$. Therefore, this loop cannot connect the stellar surface and the inner accretion disk, distant by 7.8 stellar radii, and is likely anchored on the stellar photosphere.

The high temperature and X-ray surface flux observed during the second observation point to an enhanced X-ray activity produced by a bright X-ray flare. Such bright flares on the Sun are sometimes associated with coronal mass ejection (CME). Therefore, we cannot rule out that the maximum of column density observed during the second observation is due to this energetic event.

2.4. Comparison with previous X-ray observations of AA Tau

AA Tau was previously observed several times in X-rays at different epochs: on March 4, 1980 and February 7, 1981 with the IPC on board *Einstein*, with an exposure of 0.6 h and 2.8 h, respectively; on August 10, 1990 during the *ROSAT All Sky Survey* (RASS) with the PSPC on board *ROSAT*, with an exposure of 0.2 h; and on February 22 and August 18, 1993 during two pointed PSPC observations of the young binary Haro 6-13 (PI: H. Zinnecker), with an exposure of 0.6 h and 1.5 h, respectively.

Walter & Kuhi (1981) reported a detection with $0.030 \pm 0.005\,IPC\,counts\,s^{-1}$, during the first observation with *Einstein* (bright enough to exhibit a crude spectrum), but only an upper limit of $0.004\,IPC\,counts\,s^{-1}$ with a 5 times longer observation, nearly one year later (Walter & Kuhi 1984). Walter & Kuhi (1984) associated the X-ray emission detected from AA Tau as a quiescent level, and interpreted the non-detection in the framework of the smothered coronae of TTSs (see Walter & Kuhi 1981), where it was proposed that mass ejection could increase enough the absorbing column density to smother the coronal (quiescent) X-ray emission. Neuhäuser et al. (1995) reported 10 years later a RASS detection with $0.014 \pm 0.006\,PSPC\,counts\,s^{-1}$.[6] AA Tau was also detected during the PSPC pointed observation with $0.022 \pm 0.005\,PSPC\,counts\,s^{-1}$ (see in the WGA catalogue of *ROSAT* point sources, the source 1WGA J0434.9+2428, located 37′ off-axis; White et al. 1996), but (again) only during the shortest exposure.

Further constraint can be derived on the X-ray variability of AA Tau by combining these multiple epoch observations with our better assessment of its quiescent level thanks to better spectra. For a plasma temperature $\sim 23\,MK$ and an unabsorbed X-ray luminosity in the energy band from 0.5 to 8.0 keV of $\sim 0.5 \times 10^{30}\,erg\,s^{-1}$ (equivalent to an unabsorbed X-ray flux of $2.1 \times 10^{-13}\,erg\,s^{-1}\,cm^{-2}$), absorbed by a column density of $\sim 10^{22}\,cm^{-2}$, we compute with PIMMS[7] that *Einstein*/IPC (0.2–4.5 keV) and *ROSAT*/PSPC (0.12–2.48 keV) would both observe only $\sim 0.002\,counts\,s^{-1}$. This low count rate is consistent with the

---

[4] The increase of the spectrum slope between 1 and 2 keV observed between observations #1 and #2, is not only due to the increase of the absorption, as argued in SR, but also for 20% to the increase of the plasma temperature.

[5] Reale et al. (1997) use ζ, the slope of the flare decay in a log-log diagram of the plasma temperature vs. the squared-root of the emission measure (a proxy of the plasma density), as diagnostic to assess the level of sustained heating in the analysis of stellar flares. For the *XMM-Newton* energy coverture, the corresponding range for ζ values are 0.4 and 1.9, for strongly sustained heating and freely decaying loop, respectively.

[6] Note that SR reported a RASS rate 10 times higher than the one reported by Neuhäuser et al. (1995).

[7] Available at http://asc.harvard.edu/toolkit/pimms.jsp .

IPC upper limit,[8] and we found that it is twice lower than the background level (inside a 1.5'-radius circle) at the location of AA Tau in the second PSPC pointed observation. Therefore, the previous non-detections in X-rays are consistent with the quiescent level observed with *XMM-Newton*.

We conclude that the previous X-ray detections with *Einstein*, the RASS, and *ROSAT/PSPC*, were made during high levels of activity, where AA Tau was about 18, 8, and 13 times, respectively, above its quiescent level.

2.5. XMM-Newton optical/UV monitor light curves

2.5.1. UV photometry

The OM was operated in the imaging mode default, which uses 5 imaging windows plus a small (1.7'×1.7') central imaging window. The imaging mode default consists of a sequence of 5 exposures where one of the 5 imaging windows covers a large fraction of the OM field-of-view (17'×17') with 1'' × 1'' spatial resolution, while the small central imaging window ensures a continuous monitoring of the target at the center of the field-of-view with 0.''5 × 0.''5 spatial resolution (for an illustration of this exposure sequence and a light curve obtained with the small central window see Fig. 85 of the *XMM-Newton Users' Handbook* and Grosso et al. 2007, respectively). We requested the minimum available exposure time in imaging mode default (800 s) to monitor any change in the UV photometry (UVW2 filter at 206 nm) with a ~15 min sampling rate.

We run the OM imaging mode pipeline. We made our own IDL program to plot the light curves of AA Tau from the source lists of the small central window (*OM*SWSRLI0000.FIT), and the large central window (*OM*SWSRLI1000.FIT). The latter provides *only* 1 data point per OM exposure sequence (about 5 × 800 s), which is obtained simultaneously with the first (out of 5) data point of the small central window. In a few exposures, AA Tau is missing in the observation source list of the small central window, but a visual inspection of the corresponding images confirms the detection. Therefore, we complete the light curve by doing aperture photometry.

The top panel of Fig. 1 shows the UV light curves of AA Tau. We note that the UV light curves of AA Tau reported in SR were limited to the UV photometry obtained with the large OM central imaging window (see for comparison the grey hourglasses in the top panel of our Fig. 1 and their Fig. 1). The continuous monitoring with the central window is crucial to determine accurately the UV variations on hour timescale. We find that AA Tau is variable in UV by an amount of a few 0.1 mag on a few hours timescale, and up to 1 mag on a week timescale. There are no correlation between the UV and X-ray variations.

2.5.2. Modeling of the UV variability

The UV excess observed in CTTSs is attributed to the accretion shocks at the base of the accretion funnel flows (see review on magnetospheric accretion by Bouvier et al. 2007b). Therefore, we assume that the UV flux must be somehow modulated by the warped inner disk, and we perform a least squares fitting of the UV light curve using a cosine function with free amplitude and phase, and period fixed to 8.22 days (Bouvier et al. 2007a). The resulting fit ($\chi^2 = 206.5$ for 80 d.o.f.) is not acceptable, mainly due to fast variations on day timescale that cannot be properly
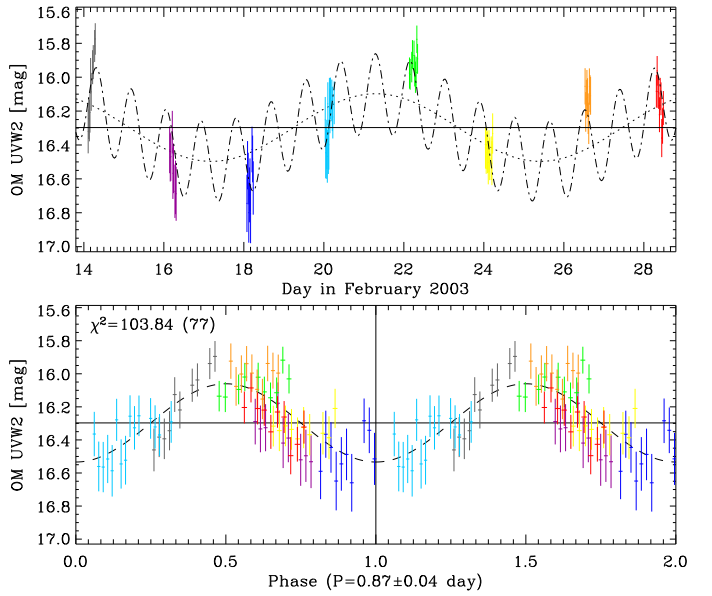
Fig. 5. Weekly and daily UV variability of AA Tau observed with the OM. Top panel: the dotted and dashed-dotted line show the weekly modulation of the UV flux attributed to the eclipse period (8.22 days), and the overall modulation of the UV flux. The horizontal line shows the average flux. Bottom panel: the dashed line shows the daily modulation of the UV folded in phase after subtraction of the weekly modulation. Symbols are the same in both panels. The formula of the overall fit (dashed-dotted line) is given by Eq. 1.

reproduced with this simple model including only weekly variations. A Lomb periodogram of the residuals suggests the presence of an additional (high-frequency) modulation with a period of 0.87 ± 0.03 day.

We then compute a grid of fits in the amplitude and phase parameter space to look for optimized values that maximize the peak of the periodogram residuals. This is equivalent to a simultaneous fitting of both modulations with the long-term period is fixed. We find a better fit ($\chi^2 = 103.8$ for 77 d.o.f.). Given the new and old values of χ^2 and number of degrees of freedom, a F-test indicates a probability of ~10^{-11} for the null hypothesis; therefore, we conclude that it is reasonnable to add this extra modulation to improve the fit. Moreover, a Lomb periodogram of the residuals shows no other modulations, and a perfect subtraction of the two modulations. The fit formula is given by the following equation:

$$UV = 16.30 \pm 0.02 \, \text{mag} \qquad (1)$$
$$+ (0.20 \pm 0.02) \cos\{2\pi[t - (17.2 \pm 0.1)]/8.22\}$$
$$+ (0.24 \pm 0.02) \cos\{2\pi[t - (14.75 \pm 0.02)]/(0.87 \pm 0.04)\},$$

where t is the day in February 2003, and the errors are given at the 68% confidence level.

The top panel of Fig. 5 shows the UV light curve and the fit given by Eq. 1. The bottom panel shows the UV light curve folded in phase with the high-frequency period after the subtraction of the long-term modulation. This light curve looks rather convincing. However, a longer UV observation with the OM is necessary to have a definitive confirmation of this high-frequency period, which would suggest a non-steady accretion.
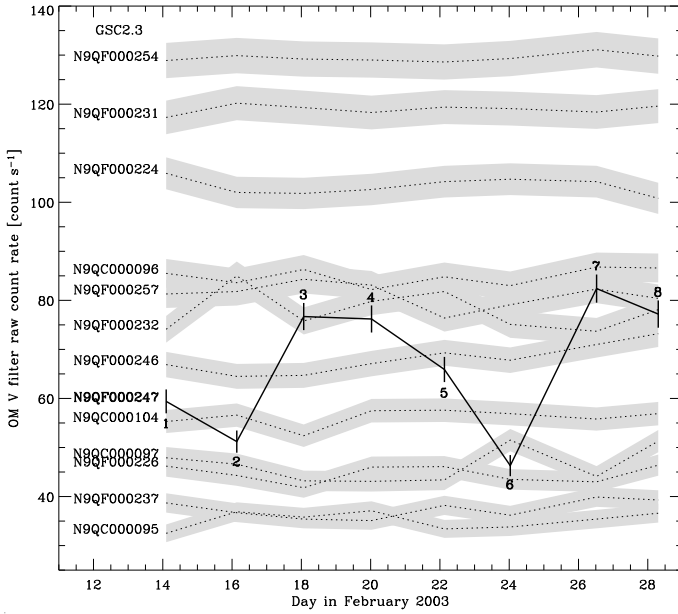
Fig. 6. Optical light curves of the OM guide stars obtained with the field acquisition exposure. The dashed lines and grey stripes indicate the raw count rates of guide stars and one-sigma variations, respectively. The thick line and error bars shows the optical light curve of AA Tau. Labels indicate counterparts in the Guide Star Catalog (version 2.3.2).

2.5.3. Optical variability from the field acquisition exposure

We propose here to obtain extra informations on the optical photometry of the target thanks to the OM Field Acquisition exposures (FAQs), where several stars are also detected in optical in the OM field of view, and are then available as comparison stars for variability study.

The FAQ is a short exposure (10 s) *V*-filter image always taken at the start of each science observation (i.e., at the beginning of the MOS observation) to allow proper identification of guide stars and to compensate small pointing errors. A thresholding is applied to the FAQ image by the OM on board software to identify guide stars. The derived offset is then applied to the OM science windows. The informations (positions in detector coordinates, count rates,...) on the guide stars are reported in the `*OMS40000RFX*` data files delivered with the Observation Data Files (ODFs). The use of the FAQ image, instead of scheduling an additional OM exposure in the imaging mode default with the *V*-filter, allowed us to make a twice longer observation with the UVW2 filter, by saving at least 5×800 s (without taking into account time overheads).

In each observation, we recover sky coordinates from detector coordinates, and identify the counterparts of guide stars in the Guide Star Catalog (version 2.3.2). Then, we build a light curve for the 13 guide stars (including AA Tau). Fig. 6 shows the variations of the raw count rates in the optical of the guide stars during our campaign. All guide stars, except AA Tau, exhibited small (lower than 2σ) relative variations in the optical. By contrast, AA Tau exhibited large relative variations, in particular, during observations #1, #2, #5, and #6 where a large dip is visible. We conclude that these 4 *XMM-Newton* observations were likely made during the optical eclipses of AA Tau.

Table 3. Journal of ground-based optical observations.

Feb. 2003 (d)	Site	Tel.	Observer	N_{obs}
13.89–28.88	Teide (Spain)	0.8 m	M.R. Z.	177
16.83–17.96	Sierra Nevada (Spain)	1.5 m	M. F.	5
20.63–28.64	Mt Maidanak (Uzbek.)	0.5 m	K. G.	8

3. UV and X-ray variabilities versus rotational phase

3.1. Ground-based optical photometry

The Journal of ground-based optical observations is given in Table 3. Observations were carried out from three sites over a time span of two weeks, covering our *XMM-Newton* observations in February 2003, using either CCD detectors or a photomultiplier tube (Mt Maidanak). Measurements were obtained in the *V* filter. Differential photometry was performed on CCD images and absolute photometry from photomultiplier observations, with an accuracy of the order of 0.01 mag. Somewhat larger systematic errors (≤ 0.05 mag) might result from the relative calibration of the photometry between sites. All data reduction procedures can be found in Bouvier et al. (2003).

The top panel of Fig. 7 shows the ground-based optical light curve; for comparison purpose, the other panels show the UV and X-ray light curves, and the plasma parameters. Unfortunately, due to bad weather conditions in Europe, none ground telescope was able to obtain simultaneous optical observations with *XMM-Newton*. In the most favorable cases, ground optical photometry was obtained only 4.3 h, 3.1 h, 2.8 h, and 2.0 h before the beginning of the MOS observations #1–#4, respectively; and only 3.3 h after the end the last MOS observation. Despite the limited time sampling, a dip, likely associated with a primary eclipse of AA Tau, is however detected at the beginning of the monitoring campaign. This supports what we deduced previously in Sect. 2.5.3 from the optical FAQ images, that *XMM-Newton* observations #1 and #2 were obtained during the eclipse. Consequently, the FAQ images can also be used safely to identify an eclipse during *XMM-Newton* observations #5 and #6, located within the Feb. 23–27, 2003 gap of the ground observation.

3.2. Folded light curves and eclipse phases

To obtain a better determination of the dates of the optical eclipses, we compare our photometry with the one obtained just 6 months apart, from Aug. 27 to Oct. 24, 2003 (Bouvier et al. 2007a). The top panel of Fig. 8 shows both photometry data set folded together in phase using the 8.22-day rotational period (Bouvier et al. 2007a), i.e., we introduced no phase difference between the two data set. The (arbitrary) common origin of phase was chosen to match the light curve of season 2003 shown in Fig. 15 of Bouvier et al. (2007a), taking the eclipse center at phase 0.5.

The behaviour of our photometry is consistent with the shape of the light curve observed during the season 2003. We can exclude any phase offset larger than 0.05 between the two epochs. A deep primary eclipse ($\Delta V \sim 1.5$ mag) is well detected at the beginning of our monitoring campaign. There is also some evidence for a shallow secondary eclipse detected only at the end of our monitoring campaign, after the last *XMM-Newton* observation. The differences in brightness of about 0.5 and 1 mag between the Feb. and Aug. 2003 data, observed at the beginning and the end of the primary eclipse, respectively, can be
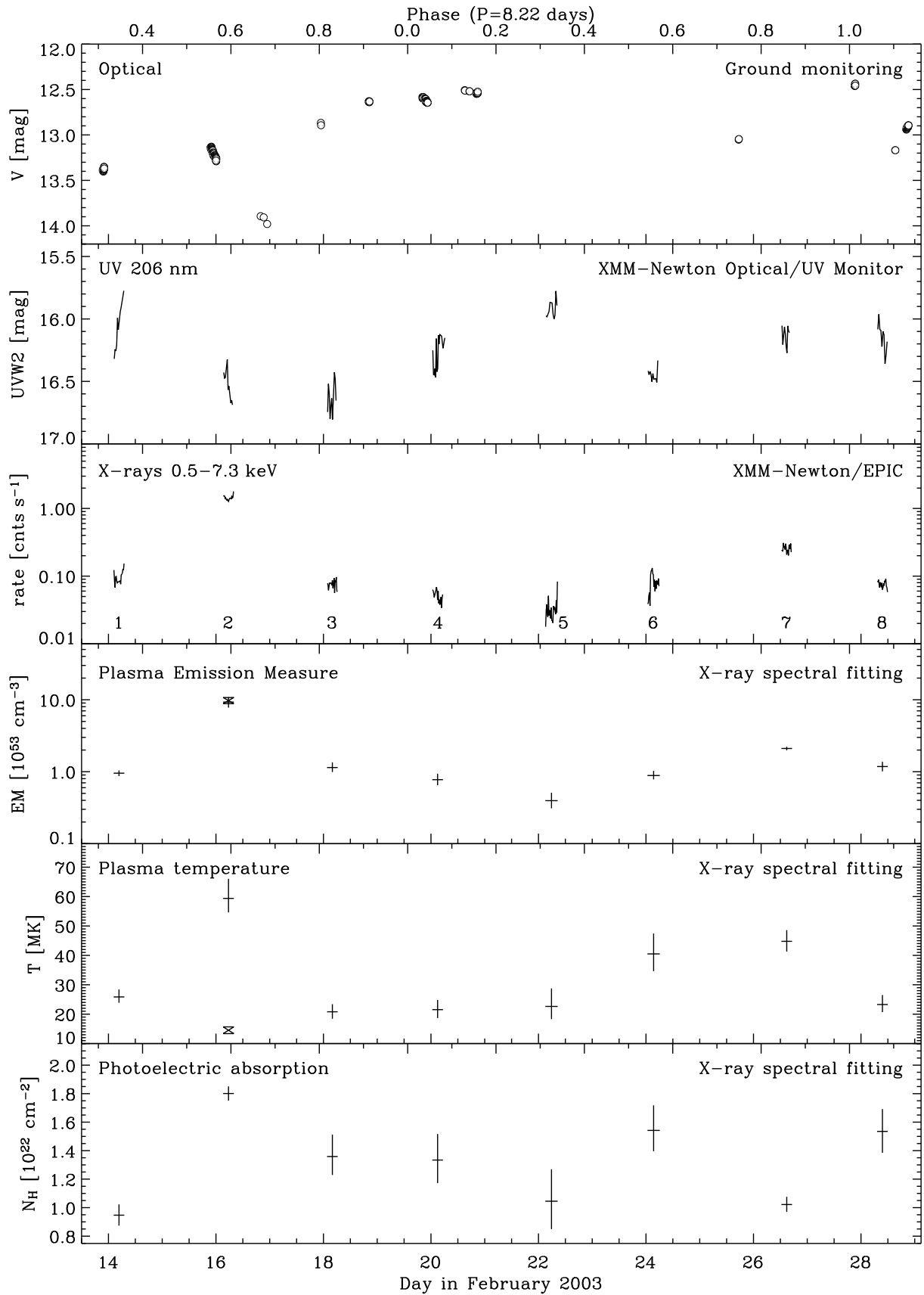
Fig. 7. Light curves and plasma parameters of AA Tau. The panels show from top to bottom: the optical, UV, and X-ray light curves (labels indicate observation numbers); the variations of the plasma emission measure(s) and temperature(s), and the photoelectric absorption (Table 2). The top horizontal axis indicates the corresponding phase for the rotation period of 8.22 days. The (arbitrary) phase origin is from Bouvier et al. (2007a).
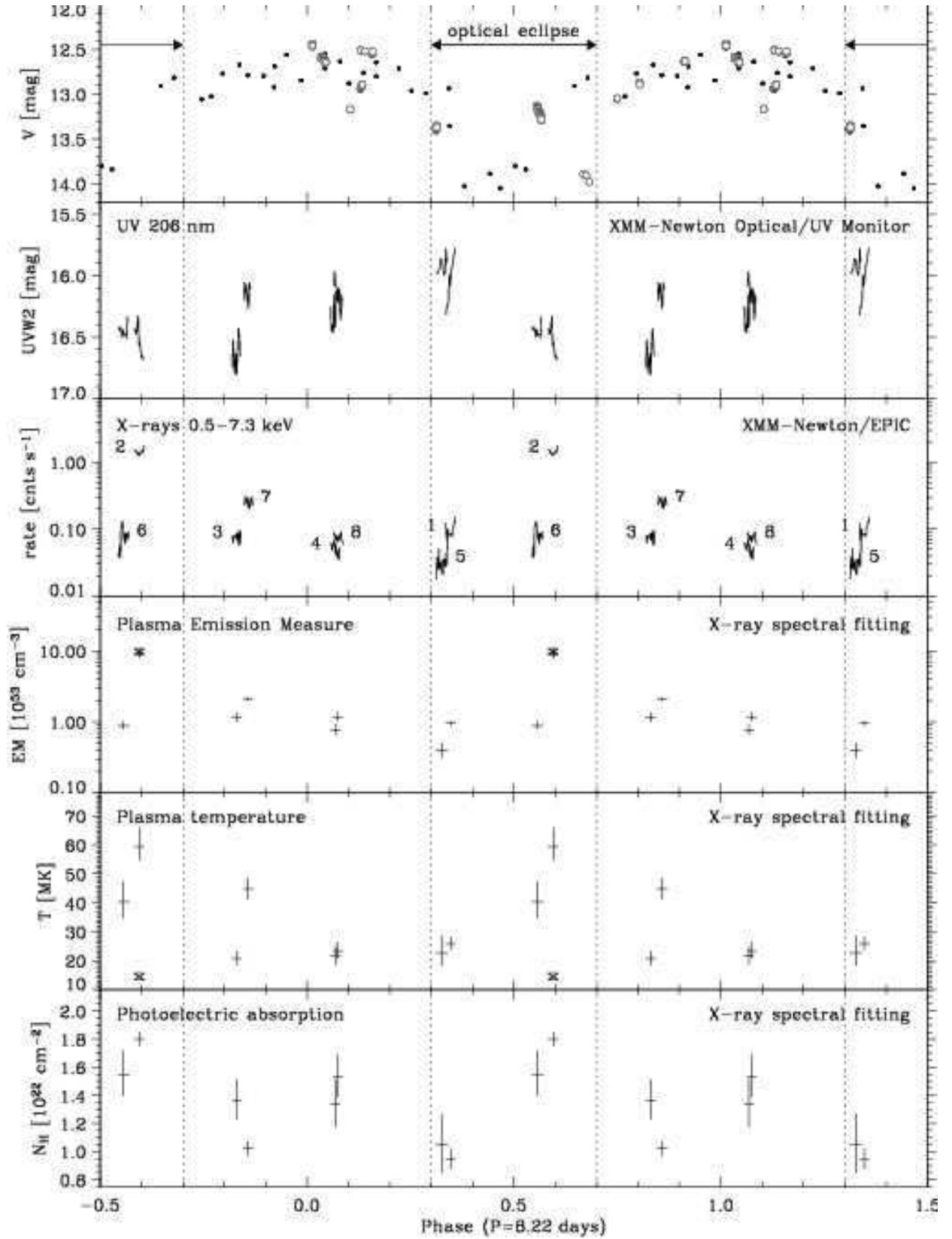
Fig. 8. Light curves and plasma parameters of AA Tau folded in phase with the rotation period of 8.22 days. Symbols and the phase origin are identical to the ones used in Fig. 7. In the top panel, black dots show for comparison the optical ground monitoring from Aug. 27 to Oct. 24, 2003 (Bouvier et al. 2007a). The horizontal arrow shows our estimate of the eclipse phase based on the optical ground monitoring.

explained with a longer duration of the eclipse in Feb. 2003. The brightening on Feb. 16, 2003, close to the center of the primary eclipse, was observed with a high sampling rate ($\sim$ 2 min), and exhibited only a fast decay. Therefore, this event is similar to the transient brightening events usually observed in the faint state of AA Tau (Bouvier et al. 1999). The primary eclipses were centered on Feb. 15.5 and Feb. 23.5, 2003, and covered phases ranging from $\sim$0.3 to $\sim$0.7. Our ground-based monitoring confirms that *XMM-Newton* observations #1, #2, #5, and #6 were made during primary eclipses. In particular, observations #2 and #6 are secured close to the center of the primary eclipse. We can exclude a secondary eclipse at the start of observations #4 and #8 thanks to the FAQ, and moreover the corresponding X-ray light curves show no decay. Therefore, we conclude that the shallow secondary eclipse likely started after the end of our observations.

The UV flux is the highest when the primary eclipse starts and the lowest towards the end of it. Indeed, the lowest UV flux was observed during the *XMM-Newton* observation #3 at the end of the egress phase, i.e., outside the primary eclipse. Our model of the UV flux variations helps to disentangle weekly modulation (produced by the warped disk) and daily variation. Eq. 1 indicates that the weekly modulation was at minimum on Feb. 17.2, 2003 (see also the top panel fo Fig. 5), which corresponds to a phase delay of about 0.2 compared to the optical eclipse. Therefore, the warped disk produces a maximum of obscuration of the UV flux at the end of the optical eclipse. Consequently, the true maximum of the UV flux occurred around phase 0.2, well before the start of the eclipse. We didn't survey this time interval with *XMM-Newton*, but we note that a brightening in the B-band of AA Tau was observed around phase 0.2 during the 1995 campaign (Bouvier et al. 1999). The delay between the optical and UV eclipse, and the smaller depth of the UV eclipse ($\Delta UVW2 \sim 0.40$ mag) compared to the optical eclipse ($\Delta V \sim 1.5$ mag), suggests a *trailing* accretion funnel flow, producing a strong absorption of the UV photons emitted at the accretion shock.

No eclipses are detected in X-rays. The variable photoelectric absorption of the X-ray spectra is not correlated with the rotational phase; similar low and high values of the column density are observed both during the eclipse and outside it. The maximum of the column density was observed at phase 0.6, close to the center of the optical eclipse, during the X-ray flare. However, increases of the column density were also reported during large stellar flares, and solar flares are sometimes associated with coronal mass ejection (see the review on X-ray astronomy of stellar coronae by Güdel 2004, and references therein). Therefore, we cannot rule out that the peak of column density is due to this energetic event. The gas column density on the line of sight produced by the warped disk is around 10^{25} cm^{-2} (Bouvier et al. 1999), which is large enough to absorb all the X-rays emitted by AA Tau, even during a bright and hot flare. The lack of eclipses in X-rays indicates that X-ray emitting regions are located above the high-density disk warp at high latitudes.

The online Fig. 9 shows the scattered plot of the average OM count rate versus the column density, where the count rate error include the observed variations of the UV flux (see Fig. 1). The correlation coefficient of this sample is -0.72, suggesting a true correlation between the two physical parameters as argued by SR, who used smaller error bars for the count rates. However, we note that the data obtained outside the eclipse are located within the cloud of points, with error bars covering all the range of observed values of column density and count rate. Therefore, the column density variation cannot be attributed to the disk warp.

Assuming a frequency of one X-ray flare per 650 ks, as observed in young solar-mass stars (Wolk et al. 2005), our 38.8 h-exposure should detect only 0.2 flare from AA Tau. The center of the optical eclipse is limited to about 0.2 in phase. Therefore, the combined probability to observe by chance an X-ray flare during the center of the transit of an accretion funnel flow is only 0.04. Moreover, the median flare level in young solar-mass stars is only 3.5 times the characteristic level (Wolk et al. 2005), whereas we observed a flare with a larger amplitude. This suggests that this event is associated with the magnetic area corresponding to the base of the dipolar magnetic field line, which controls the accretion funnel flow.

4. Discussion and conclusions

The high throughput of *XMM-Newton* allows us to obtain spectra of AA Tau at each phase of its activity. By contrast to previous *ROSAT* observations, where the measurement for this source was limited to count rate and hardness ratios in the soft X-ray energy band[9], the plasma parameters can be derived from spectral fitting, which provides, in particular, a better measurement of the column density and the X-ray luminosity.

We find that the column density, derived from the photoelectric absorption of the X-rays emitted by the active corona of AA Tau, varies from $N_H \sim 1.0 \times 10^{22}$ cm^{-2} to 1.8×10^{22} cm^{-2}. However, the optical extinction of AA Tau by the dust is very low with $A_V = 0.78$ mag (Bouvier et al. 1999), which can be converted to $N_H \sim (1.2 \pm 0.1) \times 10^{21}$ cm^{-2}, using the relation $N_H/A_J = (5.6 \pm 0.4) \times 10^{21}$ cm^{-2} mag^{-1} (Vuong et al. 2003), combined with the extinction law of Rieke & Lebofsky (1985), $A_J = 0.282 \times A_V$ (for their adopted R_V value of 3.1). We conclude that there is an excess of column density, varying from 0.9×10^{22} to 1.7×10^{22} cm^{-2}. These values are consistent with the one reported by SR. To explain this excess of column density, SR introduced an additional absorption in a disk wind (with no dust, and cool enough to avoid producing any soft X-ray emission), or a peculiar dust grain distribution with $R_V \sim 0.4$ to reconcile the observed extinction and X-ray absorption. However, we note that three-dimensional MHD simulations of disk accretion to a rotating magnetized star (e.g., Romanova et al. 2003) show that the stellar magnetosphere is far to be an empty cavity. Matter accretes mainly through narrow funnel loaded with high-density material ($\sim 10^{12}$ cm^{-3}), which are surrounded by lower density funnel flows that blanket nearly the whole magnetosphere. Therefore, we propose to identify this excess of gas with this lower density funnel flows filling the stellar magnetosphere. Dividing the excess column density by the width of the magnetosphere of AA Tau (about 7.8 stellar radii) leads to a density of a few 10^{10} cm^{-3}, which is compatible with this interpretation. Moreover, the multiple spirals visible in the simulated accretion flows should help to produce a variable column density. This low density gas, located below the radius of dust sublimation (close to the inner accretion disk for AA Tau), is then dust free.

---

[9] To convert the *ROSAT* count rate of AA Tau to X-ray luminosity, Neuhäuser et al. (1995) estimate an energy conversion factor from the visual extinction (converted to foreground hydrogen column density) and the second hardness ratio (sensitive to the plasma temperature). This leads to an X-ray luminosity of 0.4×10^{30} erg s^{-1} (see Table 1 of Johns-Krull 2007), which is likely underestimated by a factor of ten (see our simulations of count rates in Sect. 2.4), because the column density of AA Tau (see Table 2, and discussion below) is about 10 times larger than the one assumed by Neuhäuser et al. (1995).

Accreting TTSs show in average a L_X/L_{bol} ratio 2.5 times smaller than in non-accreting TTSs (see for COUP and XEST results, Preibisch et al. 2005 and Briggs et al. 2007, respectively). This is generally interpreted as a direct or indirect consequence of the accretion process (see discussion in Preibisch et al. 2005; Telleschi et al. 2007; Gregory et al. 2007). The median value of $\log(L_X/L_{bol})$ for AA Tau is -3.5; for comparison this value is intermediate between -3.7 and -3.3, the median values found for accretors and non-accretors, respectively (Preibisch et al. 2005; Briggs et al. 2007). The peculiar orientation of AA Tau may help to overcome partly the extinction by the accretion funnels (Gregory et al. 2007).

Recently, Johns-Krull (2007) reported new magnetic field measurements for CTTSs, based on Zeeman broading of photospheric absorption lines in the near-IR, showing that the observed mean magnetic field is in all cases greater than the field predicted by pressure equipartition arguments. Johns-Krull (2007) suggests that the very strong fields decrease on these stars the efficiency with which convective gas motions in the photosphere can tangle magnetic loops in the corona. For AA Tau, Johns-Krull (2007) reports a value of 2.78 kG for the mean magnetic field, that is 2.7 times larger than the field strength at pressure equipartition; and predicts from solar scaling an (unobserved) X-ray luminosity of about 4×10^{30} erg s^{-1} (for comparison this value is 10 times greater than the minimum level that we observed). However, our observation shows that a bright X-ray flare can occur during the transit of an accretion funnel flow, and locate the active X-ray area likely close to the foot of the accretion funnel flow. We speculate that a magnetic interaction exists between the free falling accretion flow and the strong magnetic field of the stellar corona, which may trigger magnetic reconnections and give rise to bright X-ray flares, which boost the X-ray emission.

This campaign of observations of AA Tau with *XMM-Newton* shows that X-ray spectroscopy with CCD provides a unique tool to probe the circumstellar dust-free gas in this object, and that some magnetic flares are likely associated with the accretion process. Longer coordinated optical and X-ray/UV observations of AA Tau are still needed to obtain continuous light curves, which is crucial to confirm the flaring behaviour of active regions associated with the accretion funnel flow, and daily modulation of the UV flux. Simultaneous Zeeman-Doppler images would help to derive a surface magnetogram; this map of the magnetic active regions on the stellar photosphere, combined with the X-ray light curves, would then allow to build a self-consistent three-dimensional model of the corona of AA Tau.

Taking into account that the duration of the visibility window for AA Tau is about 130 ksec per *XMM-Newton* orbit (2 days), a full monitoring of two optical eclipse periods of AA Tau (8.22 days) with *XMM-Newton* is equivalent to an effective exposure of 1.1 million seconds. This project has the typical duration of the large programs which are anticipated with *XMM-Newton* for the next decade.

References

Anders, E. & Grevesse, N. 1989, Geochim. Cosmochim. Acta, 53, 197

Argiroffi, C., Maggio, A., & Peres, G. 2007, A&A, 465, L5

Asplund, M., Grevesse, N., & Sauval, A. J. 2005, in ASP Conf. Ser. 336: Cosmic Abundances as Records of Stellar Evolution and Nucleosynthesis, ed. T. G. Barnes, III & F. N. Bash, 25–39

Audard, M., Skinner, S. L., Smith, K. W., Güdel, M., & Pallavicini, R. 2005, in Proceedings of the 13th Cambridge Workshop on Cool Stars, Stellar Systems and the Sun, ESA SP-560, ed. F. Favata et al., 411–415

Bouvier, J., Alencar, S. H. P., Boutelier, T., et al. 2007a, A&A, 463, 1017

Bouvier, J., Alencar, S. H. P., Harries, T. J., Johns-Krull, C. M., & Romanova, M. M. 2007b, in Protostars and Planets V, ed. B. Reipurth, D. Jewitt, & K. Keil, 479–494

Bouvier, J., Chelli, A., Allain, S., et al. 1999, A&A, 349, 619

Bouvier, J., Grankin, K. N., Alencar, S. H. P., et al. 2003, A&A, 409, 169

Briggs, K. R., Güdel, M., Telleschi, A., et al. 2007, A&A, 468, 413

Broos, P. S., Feigelson, E. D., Townsley, L. K., et al. 2007, ApJS, 169, 353

Dorman, B. & Arnaud, K. A. 2001, in ASP Conf. Ser. 238: Astronomical Data Analysis Software and Systems X, ed. F. R. Harnden, Jr., F. A. Primini, & H. E. Payne, 415–418

Favata, F., Flaccomio, E., Reale, F., et al. 2005, ApJS, 160, 469

Feigelson, E. D. & Montmerle, T. 1999, ARA&A, 37, 363

Getman, K. V., Feigelson, E. D., Grosso, N., et al. 2005a, ApJS, 160, 353

Getman, K. V., Flaccomio, E., Broos, P. S., et al. 2005b, ApJS, 160, 319

Gregory, S. G., Wood, K., & Jardine, M. 2007, ArXiv e-prints, 704

Grosso, N., Audard, M., Bouvier, J., Briggs, K. R., & Güdel, M. 2007, A&A, 468, 557

Grosso, N., Montmerle, T., Feigelson, E. D., & Forbes, T. G. 2004, A&A, 419, 653

Güdel, M. 2004, A&A Rev., 12, 71

Güdel, M., Arzner, K., Audard, M., & Mewe, R. 2003, A&A, 403, 155

Güdel, M., Audard, M., Magee, H., et al. 2001, A&A, 365, L344

Güdel, M., Briggs, K. R., Arzner, K., et al. 2007a, A&A, 468, 353

Güdel, M., Skinner, S. L., Mel'Nikov, S. Y., et al. 2007b, A&A, 468, 529

Guenther, E. W., Lehmann, H., Emerson, J. P., & Staude, J. 1999, A&A, 341, 768

Günther, H. M., Schmitt, J. H. M. M., Robrade, J., & Liefke, C. 2007, A&A, 466, 1111

Imanishi, K., Nakajima, H., Tsujimoto, M., Koyama, K., & Tsuboi, Y. 2003, PASJ, 55, 653

Jansen, F., Lumb, D., Altieri, B., et al. 2001, A&A, 365, L1

Johns-Krull, C. M. 2007, ApJ, 664, 975

Johns-Krull, C. M., Valenti, J. A., & Koresko, C. 1999, ApJ, 516, 900

Johns-Krull, C. M., Valenti, J. A., & Saar, S. H. 2004, ApJ, 617, 1204

Kastner, J. H., Huenemoerder, D. P., Schulz, N. S., Canizares, C. R., & Weintraub, D. A. 2002, ApJ, 567, 434

Kenyon, S. J., Dobrzycka, D., & Hartmann, L. 1994, AJ, 108, 1872

Mason, K. O., Breeveld, A., Much, R., et al. 2001, A&A, 365, L36

Ménard, F., Bouvier, J., Dougados, C., Mel'nikov, S. Y., & Grankin, K. N. 2003, A&A, 409, 163

Morrison, R. & McCammon, D. 1983, ApJ, 270, 119

Ness, J.-U., Güdel, M., Schmitt, J. H. M. M., Audard, M., & Telleschi, A. 2004, A&A, 427, 667

Neuhäuser, R., Sterzik, M. F., Schmitt, J. H. M. M., Wichmann, R., & Krautter, J. 1995, A&A, 297, 391

Ozawa, H., Grosso, N., & Montmerle, T. 2005, A&A, 429, 963

Porquet, D., Mewe, R., Dubau, J., Raassen, A. J. J., & Kaastra, J. S. 2001, A&A, 376, 1113

Preibisch, T., Kim, Y.-C., Favata, F., et al. 2005, ApJS, 160, 401

Reale, F., Betta, R., Peres, G., Serio, S., & McTiernan, J. 1997, A&A, 325, 782

Rieke, G. H. & Lebofsky, M. J. 1985, ApJ, 288, 618

Robrade, J. & Schmitt, J. H. M. M. 2006, A&A, 449, 737

Romanova, M. M., Ustyugova, G. V., Koldoba, A. V., Wick, J. V., & Lovelace, R. V. E. 2003, ApJ, 595, 1009

Scargle, J. D. 1998, ApJ, 504, 405

Schmitt, J. H. M. M. & Favata, F. 1999, Nature, 401, 44

Schmitt, J. H. M. M., Ness, J.-U., & Franco, G. 2003, A&A, 412, 849

Schmitt, J. H. M. M. & Robrade, J. 2007, A&A, 462, L41

Schmitt, J. H. M. M., Robrade, J., Ness, J.-U., Favata, F., & Stelzer, B. 2005, A&A, 432, L35

Smith, K., Audard, M., Güdel, M., Skinner, S., & Pallavicini, R. 2005, in Proceedings of the 13th Cambridge Workshop on Cool Stars, Stellar Systems and the Sun, ESA SP-560, ed. F. Favata et al., 971–975

Stassun, K. G., van den Berg, M., & Feigelson, E. 2007, ApJ, 660, 704

Stelzer, B. & Schmitt, J. H. M. M. 2004, A&A, 418, 687

Strüder, L., Briel, U., Dennerl, K., et al. 2001, A&A, 365, L18

Telleschi, A., Güdel, M., Briggs, K. R., Audard, M., & Scelsi, L. 2007, A&A, 468, 443

Turner, M. J. L., Abbey, A., Arnaud, M., et al. 2001, A&A, 365, L27

Vuong, M. H., Montmerle, T., Grosso, N., et al. 2003, A&A, 408, 581

Walter, F. M. & Kuhi, L. V. 1981, ApJ, 250, 254
Walter, F. M. & Kuhi, L. V. 1984, ApJ, 284, 194
Wang, J., Townsley, L. K., Feigelson, E. D., et al. 2007, ApJS, 168, 100
White, N. E., Giommi, P., & Angelini, L. 1996, VizieR Online Data Catalog
Wilms, J., Allen, A., & McCray, R. 2000, ApJ, 542, 914
Wolk, S. J., Harnden, F. R., Flaccomio, E., et al. 2005, ApJS, 160, 423
Yang, H., Johns-Krull, C. M., & Valenti, J. A. 2005, ApJ, 635, 466

Online Material

Appendix A: Elemental abundances of the coronal plasma and the absorbing material

The typical values of plasma element abundances observed in the coronae of young stars with fine X-ray spectroscopy (Güdel et al. 2007a), that we use for the `vapec` coronal plasma model in our X-ray spectral fitting with `XSPEC`, are given in Col. (2)–(4) of Table A.1.

The column density of the absorbing material located on the line of sight is estimated from spectral fitting using a photoelectric absorption model, that uses photoionization cross sections, and solar abundances for the material composition. The `wabs` photoelectric absorption model use photoionization cross sections of Morrison & McCammon (1983), and (old) solar abundances of Anders & Grevesse (1989). Significant revisions of the solar abundances have been made recently, as a result of the application of a time-dependent, 3D hydrodynamical model of the solar atmosphere, instead of 1D hydrostatic models. This has decreased the metal abundances, in particular of carbon and oxygen, which are the main contributor to the photoionization cross section above 0.3 and 0.6 keV, respectively. Consequently, the absolute value of the column density is dependent of the adopted photoelectric absorption model. Using updated solar abundances is then crucial when the absolute value of the column density is needed (e.g., Vuong et al. 2003). Col. (5)–(7) of Table A.1 give the recent compilation of elemental solar abundances by Asplund et al. (2005), where the decrease of metal by comparison with Anders & Grevesse (1989) is indicated in the last column.

We test the impact of these udpated solar abundances on our fitting by replacing `wabs` by `tbvarabs` (Wilms et al. 2000), which allows to input new abundances for the absorbing material. Moreover, `tbvarabs` uses also updated photoionization cross sections. We find nearly identical values of temperature and emission measure, however, as anticipated the column density value is increased. Fig. A.1 shows that column density values obtained with `wabs` are underestimated by about 50%.

Table A.1. Elemental abundances of the coronal plasma and the absorbing material.

El (1)	Coronal plasma[a]			Absorbing material[b]		
	A(El) (2)	n(El)$/n$(H) (3)	angr (4)	A(El) (5)	n(El)$/n$(H) (6)	angr (7)
He	10.99	9.77E-02	1.000	10.93	8.51E-02	0.871
C	8.21	1.63E-04	0.450	8.39	2.45E-04	0.676
N	7.95	8.83E-05	0.788	7.78	6.03E-05	0.538
O	8.56	3.63E-04	0.426	8.66	4.57E-04	0.537
Ne	8.01	1.02E-04	0.832	7.84	6.92E-05	0.562
Na	.....	....	.....	6.17	1.48E-06	0.691
Mg	7.00	9.99E-06	0.263	7.53	3.39E-05	0.892
Al	6.17	1.47E-06	0.500	6.37	2.34E-06	0.795
Si	7.04	1.10E-05	0.309	7.51	3.24E-05	0.912
S	6.83	6.76E-06	0.417	7.14	1.38E-05	0.852
Cl	.....	....	.....	5.50	3.16E-07	1.682
Ar	6.30	2.00E-06	0.550	6.18	1.51E-06	0.417
Ca	5.65	4.47E-07	0.195	6.31	2.04E-06	0.892
Cr	.....	....	.....	5.64	4.37E-07	0.902
Fe	6.96	9.13E-06	0.195	7.45	2.82E-05	0.602
Co	.....	....	.....	4.92	8.32E-08	0.967
Ni	5.54	3.47E-07	0.195	6.23	1.70E-06	0.954

Notes: Col. (2) and (5) give the element abundances on the logarithmic astronomical scale, where the numbers of hydrogen atoms are set to A(H) $= \log n$(H) $= 12$. The numbers of element atoms normalized to the number of hydrogen atoms are given in Col. (3) and (6); Col. (4) and (7) compare this ratio to Anders & Grevesse (1989)'s photospheric abundances.

[a] Elemental abundances observed in the coronae of young stars with fine X-ray spectroscopy (Güdel et al. 2007a) used in `vapec`.
[b] Elemental solar abundances of Asplund et al. (2005) used in `tbvarabs`.
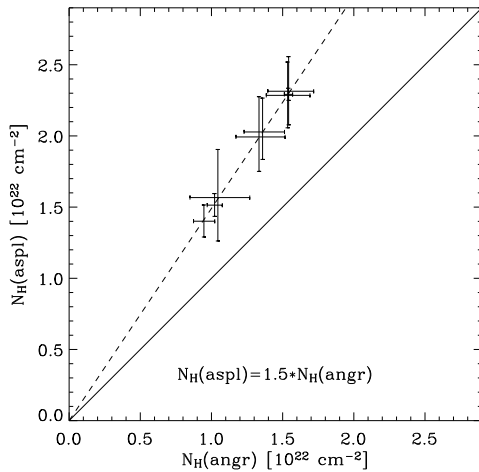
List of Objects

Fig. A.1. Comparison of the column density values obtained from spectral fitting when using the old (Anders & Grevesse 1989) and the updated (Asplund et al. 2005) solar abundances. The dashed line shows the mean average between the two values of column density.
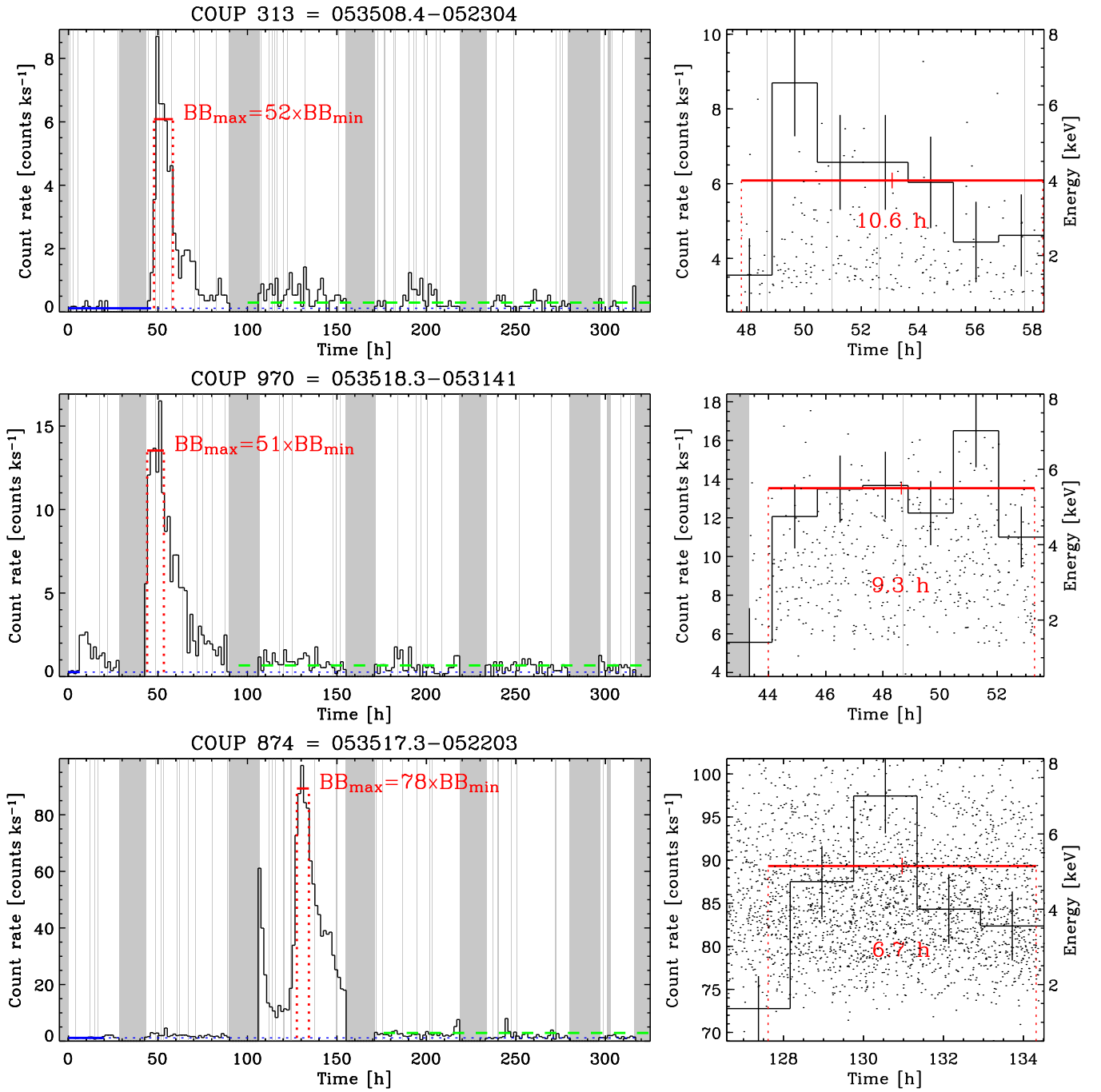
Fig. 2. A subset of X-ray flares from the *Chandra Orion Ultradeep Project* with peak amplitude and duration larger than the one observed in AA Tau. The left panels show COUP light curves (see Getman et al. 2005b), where blue and red segments indicate the minimum (BB_{min}) and maximum (BB_{max}) levels obtained from Bayesian block analysis (Scargle 1998), respectively. The blue dotted line show the minimum level. The peak amplitudes are also given. The dashed green lines start 1.7 days after the end of the maximum Bayesian block, and indicate the level (2.5 times above the minimum level), that was observed in the third observation of AA Tau. The right panels are an enlargement of the light curve around the Bayesian block showing the peak level and duration. Dots mark the arrival times of individual X-ray photons with their corresponding energies given on the right-hand axis. Large vertical gray stripes indicate the five passages of *Chandra* through the van Allen belts where ACIS was taken out of the focal plane and thus was not observing Orion.
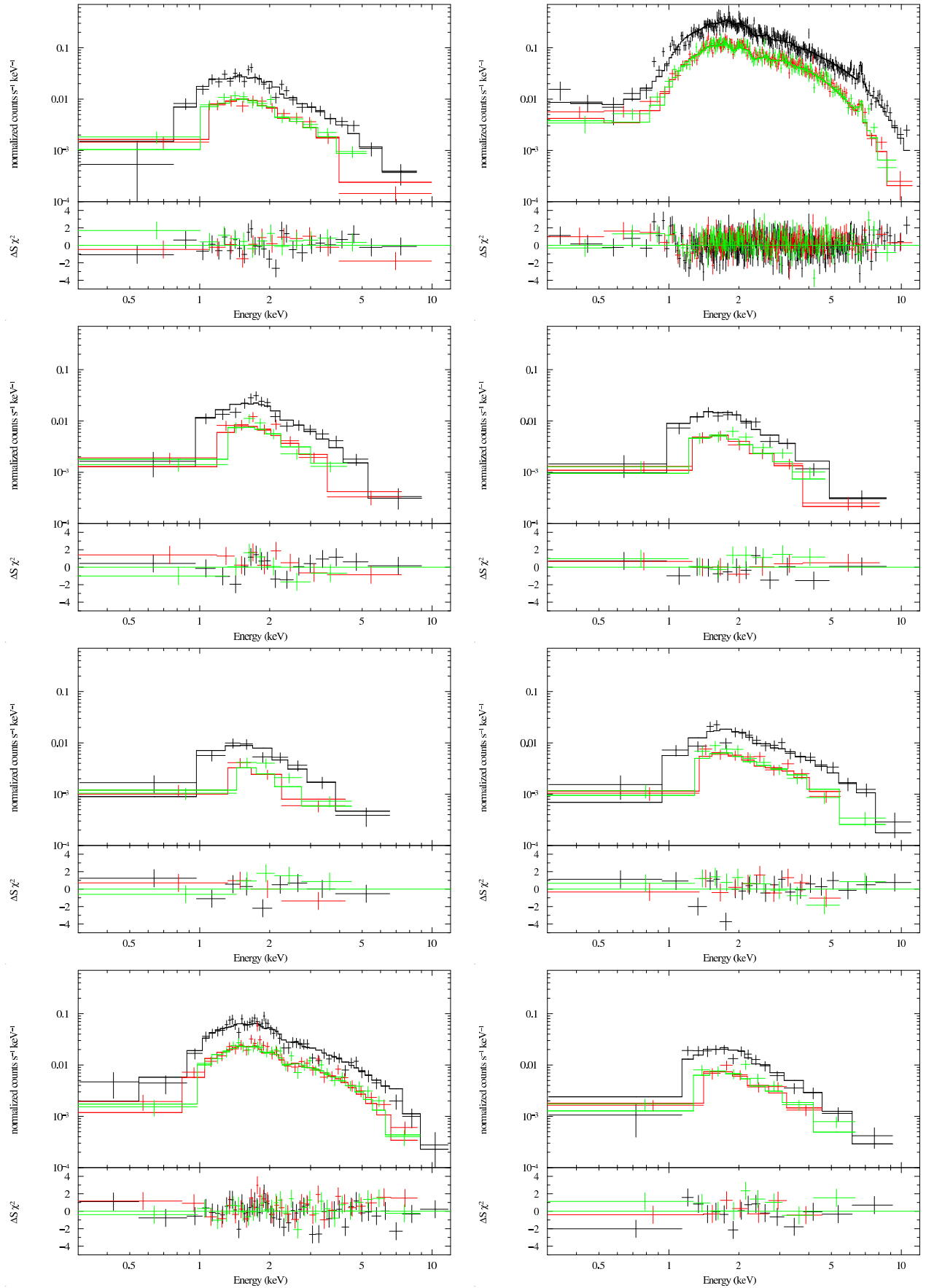
Fig. 3. EPIC pn (black), MOS1 (red), MOS2 (green) spectra of AA Tau plotted with the same scale. The lines show our best fits using one-temperature plasma combined with photoelectric absorption for observations #1 to #8 (Table 2) from left to right and top to bottom. The residuals are plotted in terms of sigmas with error bars of size one.
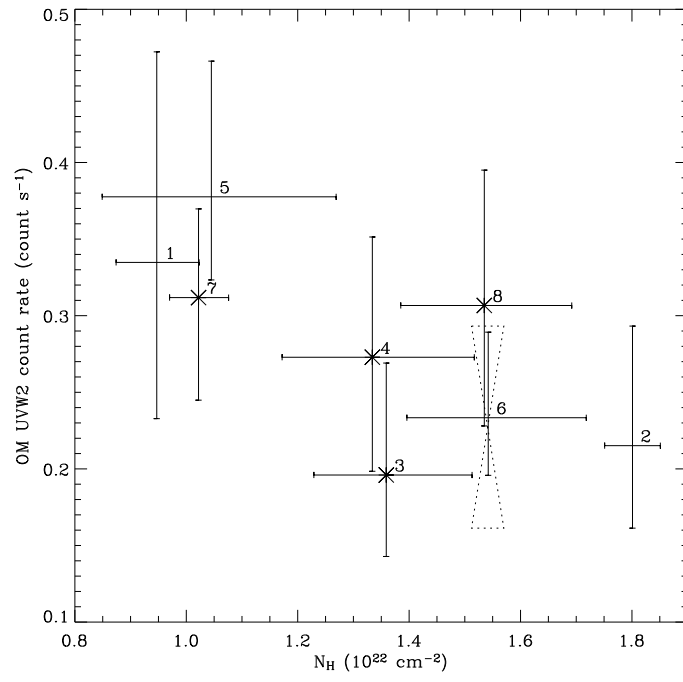
Fig. 9. Average OM count rate versus column density. Labels indicate *XMM-Newton* observations. The crosses mark observations obtained outside the optical eclipse. The dotted hourglass shows the column density of observation #2 when using only one-temperature plasma.